

Formation of buffer-gas-trap based positron beams

M. R. Natisin,^{a)} J. R. Danielson,^{b)} and C. M. Surko^{c)}

Department of Physics, University of California, San Diego, La Jolla, California 92093, USA

(Received 24 October 2014; accepted 6 February 2015; published online 2 March 2015)

Presented here are experimental measurements, analytic expressions, and simulation results for pulsed, magnetically guided positron beams formed using a Penning-Malmberg style buffer gas trap. In the relevant limit, particle motion can be separated into motion along the magnetic field and gyro-motion in the plane perpendicular to the field. Analytic expressions are developed which describe the evolution of the beam energy distributions, both parallel and perpendicular to the magnetic field, as the beam propagates through regions of varying magnetic field. Simulations of the beam formation process are presented, with the parameters chosen to accurately replicate experimental conditions. The initial conditions and ejection parameters are varied systematically in both experiment and simulation, allowing the relevant processes involved in beam formation to be explored. These studies provide new insights into the underlying physics, including significant adiabatic cooling, due to the time-dependent beam-formation potential. Methods to improve the beam energy and temporal resolution are discussed. © 2015 AIP Publishing LLC.

[<http://dx.doi.org/10.1063/1.4913354>]

I. INTRODUCTION

Positron interactions with ordinary matter are important in a variety of contexts, including atomic physics, material science, astrophysics, and medicine.^{1–4} Unfortunately, the range of experimental data available regarding fundamental positron-matter interactions is severely limited as compared, for example, to analogous electron-matter processes. This difference is due largely to the difficulties encountered in obtaining large numbers of low energy positrons. While electron sources are capable of producing fluxes of $\sim 10^{15} \text{ s}^{-1}$ at electron volt energies, typical positron sources are limited to $\sim 10^7 \text{ s}^{-1}$, making sacrificial trapping and energy-selection techniques impractical.

Positron beams can be created by implanting the positrons emitted from a radioactive source into a thin layer of material, called a moderator, which thermalizes and subsequently ejects a small fraction of the positrons at electron volt energies.⁵ However, these beams typically have energy spreads of several hundred milli-electron volts.⁶ The development of magnetically guided trap-based beams led to significant improvements in beam energy resolution,^{7,8} with the buffer gas trap (BGT) the method of choice for trapping and forming these low energy beams.⁹

The BGT is capable of producing pulsed, magnetically guided positron beams tunable from 0.1 eV to keV energies, and is now used in a wide variety of applications, including antihydrogen,^{10–13} formation of dense gases of positronium atoms,¹⁴ material science,¹⁵ and atomic physics studies.^{1,16} Using these techniques, positron beams with tens of milli-electron volt energy spreads and sub-microsecond temporal spreads are routinely produced.^{7,8} Although these resolutions are sufficient for probing well isolated processes at

energies $\geq 50 \text{ meV}$, many processes are still difficult or impossible to study without further advancements in beam technology.

For example, while studies of vibrational excitation by positron impact have been carried out for a small selection of molecules,^{17,18} there are as yet no direct measurements of state-resolved rotational excitation. Additionally, well isolated features, such as vibrational Feshbach resonances (VFRs), created by the excitation of fundamental molecular vibrational modes, have been studied,¹ while more dense vibrational spectra have yet to be investigated.^{19–21}

More generally, although techniques for trap-based beams have been devised to optimize specific beam parameters (e.g., narrow energy spreads,⁷ time-compression of beam pulses,²² and small diameter beam extraction²³), there have been few systematic studies of the relevant beam formation processes, or how beam quality depends on them. A better understanding of beam formation will aid in the development of improved and novel experimental techniques and technology that, in turn, can then be expected to enable study of a variety of additional phenomena.

Presented here is a description of experimental techniques and measurements of positron beam formation from a Penning-Malmberg style buffer gas trap. This study elucidates the role of key experimental parameters under a variety of beam formation conditions, allowing for a description of the conditions and parameters relevant to the quality of the resulting beam to be developed. Also described is a model of the beam-energy distribution, from which analytic expressions for the energy distributions, both along and in the plane perpendicular to the magnetic field, are developed. Simulation results for the beam formation process are also presented that are designed to replicate the experimental conditions as accurately as possible, and they provide more detailed insights into the underlying physics than that can be gained from experiment alone.

^{a)}Electronic mail: mnatisin@physics.ucsd.edu

^{b)}Electronic mail: jdaniel@physics.ucsd.edu

^{c)}Electronic mail: csurko@ucsd.edu

This paper is organized as follows. Section II provides a description of experimental procedures and conditions, including a model of the beam-energy distribution, followed by a discussion of the techniques used to measure the key beam characteristics. Section III describes the simulations, including a discussion of the dynamical processes involved in beam formation and transport. The experimental and simulation results are compared using a variety of beam formation conditions in Sec. IV, and the underlying processes responsible for beam quality are discussed. The paper ends with a set of concluding remarks.

II. EXPERIMENTAL STUDIES

A. Positron trapping and beam formation

The experimental apparatus has been described in detail elsewhere.¹ High energy positrons from a ^{22}Na radioactive source are moderated by inelastic collisions with a thin layer of solid Ne at ~ 8 K, slowing the positrons to electron volt energies. These moderated positrons are then magnetically guided into a three stage BGT.

The BGT consists of a modified Penning-Malmberg trap in a ~ 0.1 T magnetic field. The electrodes are cylindrically symmetric, with each of the three stages having successively larger diameters. Molecular nitrogen is injected into the first stage and maintained at lower pressures in the other two stages through differential pumping with typical N_2 pressures of 10^{-3} , 10^{-4} , and 10^{-6} Torr in stages I, II, and III, respectively. The voltages applied to the electrodes are such that the potential steps to lower values in each successive stage with a potential barrier at the end of stage III to prevent the positrons from escaping the trap. The high N_2 pressure in stage I enables good trapping efficiency ($\sim 30\%$), while the low pressure in stage III minimizes losses due to annihilation.

Positrons enter the trap on the high pressure side and lose energy primarily through electronic excitation of the N_2 , eventually becoming confined in a potential well in the third stage. Approximately $1\ \mu\text{Torr}$ of carbon tetrafluoride is injected into the third stage, allowing the positrons to more quickly cool to the gas temperature through vibrational excitation of the CF_4 . After a cool time of 100 ms, the trapped 300 K positron cloud is formed into a beam.

The potentials used to confine and eject the positrons from Stage III are shown schematically in Fig. 1. They are generated by three sets of electrodes. The outer two sets, labeled V_T and V_E , determine the trapping-gate and exit-gate potentials. These potentials provide axial confinement, and are held fixed during beam formation with $V_E < V_T$ to give a directionality to the ejected beam. The center set of electrodes then provides the well potential, V_W , setting the well depth $V_E - V_W$. The positrons are ejected by increasing V_W , lifting the positrons over V_E to form a pulsed positron beam.

An example of the voltage applied to the well electrode during a typical pulse is shown in Fig. 2. The well voltage is raised by setting a higher voltage on an amplifier. The resulting voltage ramp can be modeled as the resistance-

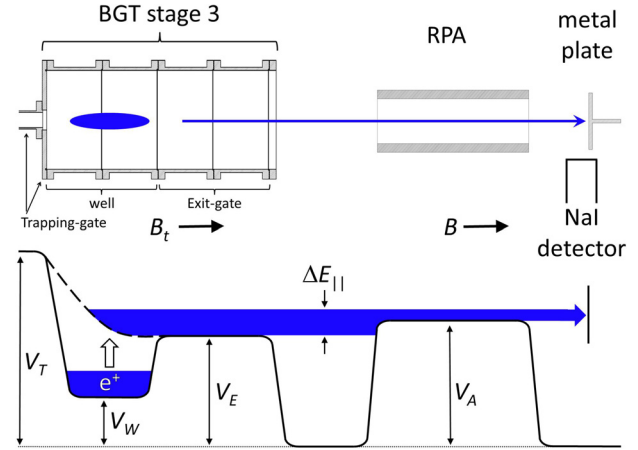


FIG. 1. Schematic diagram of (top) experimental components and (bottom) potentials used to measure the beam parallel energy distribution. Cooled positrons are initially confined in a potential well in the third stage of the BGT. V_W is then increased, lifting the positrons over V_E , forming a beam with parallel energy spread ΔE_{\parallel} . The beam is passed through an RPA, allowing only positrons with $E_{\parallel} > V_A$ to be annihilated on a metal plate and counted using a NaI detector. This process is repeated at a variety of V_A values, allowing the cumulative parallel energy distribution to be constructed.

capacitance (rc) response of an electrode to an applied voltage

$$V_W(t) = (V_s - V_0) \left[1 - \exp\left(\frac{-t}{\tau_r}\right) \right] + V_0, \quad (1)$$

where V_s is the final steady-state voltage, V_0 is the initial (well) voltage, and τ_r is the rc response time.

The initial well voltage affects the initial well depth, with the time dependence of positron ejection set by V_s and τ_r . While the voltage on the electrode eventually reaches V_s , the positrons are ejected from the trap at $V_W \sim V_E$, which typically occurs before V_s is reached. Consequently, both V_s and τ_r affect how quickly the well voltage reaches V_E . However, V_s is chosen experimentally, while τ_r is set by the resistance and capacitance of the amplifier-electrode circuit. Shown for comparison in Fig. 2 is the solution to Eq. (1) with $V_s = 3.5$ V, $V_0 = 0$ V, and $\tau_r = 10\ \mu\text{s}$. The rise time $\tau_r = 10\ \mu\text{s}$ was held fixed for all experiments discussed here.

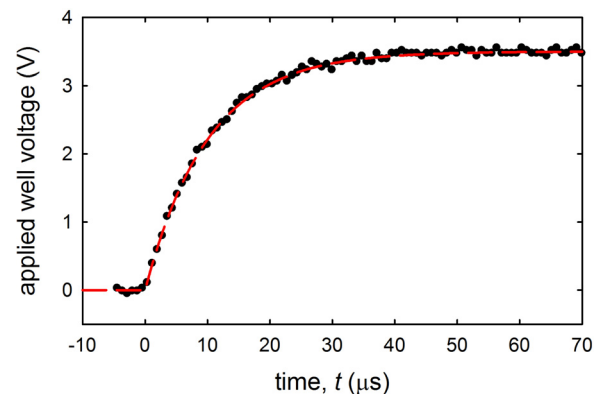


FIG. 2. Time-dependent voltage applied to well electrodes during positron ejection. (●) Applied voltage as measured on an oscilloscope and (—) Eq. (1) with $V_s = 3.5$ V, $V_0 = 0$ V, and $\tau_r = 10\ \mu\text{s}$.

B. Modeling the beam energy distribution

For the beams described here, the particles experience changes in the magnetic field on a time scale slow compared to the period of the cyclotron motion. This allows the orbits to be described using a guiding center approximation in which the centers of the cyclotron orbits follow magnetic field lines. In this case, the particle motion can be decomposed into two components: one parallel to the magnetic field, and the so-called gyro-motion perpendicular to it. A key feature of the dynamics is that the orbital magnetic moment of the positron, μ , is an adiabatic invariant of the system, defined (in S.I. units) as

$$\mu = \frac{mv_{\perp}^2}{2B} = E_{\perp}/B. \quad (2)$$

Here, m , v_{\perp} , and E_{\perp} are the positron mass, perpendicular velocity, and perpendicular energy, respectively, and B is the magnetic field at the location of the positron. The invariance of μ implies that, as the positron enters regions of lower (higher) magnetic field, its perpendicular energy decreases (increases) proportionally. Conservation of energy then requires that a decrease in perpendicular energy, for example, is accompanied by an increase in the positron parallel energy. This leads to a correlation of the parallel and perpendicular energies as the positron travels through regions of varying magnetic field.

Since the total energy distribution of the beam includes both the parallel and perpendicular motion, it is most easily understood by separately analyzing the constituent components. The parallel energy distribution, as will be shown, is largely set by beam formation processes, such as the geometry of the trapping well and the speed at which the positrons are ejected. In contrast, because of the invariance of μ , the perpendicular distribution is independent of the manner in which the beam is formed, and depends only on the initial positron temperature and magnetic field.

Experimental measurements and simulations (presented below) show that under the conditions discussed here, the parallel energy distribution closely resembles a Gaussian distribution

$$f(E_{\parallel}) = \frac{1}{\sqrt{2\pi}\sigma_0} \exp\left[-\frac{(E_{\parallel} - \bar{E}_0)^2}{2\sigma_0^2}\right], \quad (3)$$

where E_{\parallel} represents the positron energy parallel to the magnetic field, and σ_0 and \bar{E}_0 are the standard deviation and mean of the Gaussian distribution. It should be noted that simulations indicate the use of other ramp protocols and/or non-parabolic potential wells can result in non-Gaussian parallel energy distributions.

In contrast to the parallel energy distribution, because the beam formation does not affect the perpendicular energy distribution of the beam, it is well described by a Maxwell-Boltzmann (MB) distribution in two dimensions

$$f(E_{\perp}) = \frac{1}{k_b T_{\perp}} \exp\left[-\frac{E_{\perp}}{k_b T_{\perp}}\right], \quad (4)$$

where E_{\perp} and T_{\perp} represent the positron energy and temperature perpendicular to the magnetic field, and k_b is Boltzmann's constant.

Since the positron energies parallel and perpendicular to the magnetic field are well described by Gaussian and MB distributions, respectively, the beam is modeled using a joint energy distribution function, $f(E_{\parallel}, E_{\perp})$, which is the product of Eqs. (3) and (4).²⁴ The total energy distribution is obtained by convolving $f(E_{\parallel}, E_{\perp})$ with an energy conserving delta function, $\delta(E_{\parallel} + E_{\perp} - E_t)$, where E_t represents the positron total energy, yielding an exponentially-modified Gaussian distribution (EMG),²⁴

$$f(E_t) = \frac{1}{2k_b T_{\perp}} \exp\left[\frac{1}{k_b T_{\perp}} \left(\bar{E}_0 + \frac{\sigma_0^2}{2k_b T_{\perp}} - E_t\right)\right] \times \operatorname{erfc}\left[\frac{1}{\sqrt{2}\sigma_0} \left(\bar{E}_0 + \frac{\sigma_0^2}{k_b T_{\perp}} - E_t\right)\right]. \quad (5)$$

Here, erfc is the complementary error function with \bar{E}_0 and σ_0 the mean and standard deviation of the Gaussian component of the distribution, as in Eq. (3). The mean and standard deviation of the overall total energy distribution are

$$\bar{E}_t = \bar{E}_0 + k_b T_{\perp} \quad (6)$$

and

$$\sigma_t = \sqrt{\sigma_0^2 + (k_b T_{\perp})^2}. \quad (7)$$

The above characterization of the BGT-based beam has been described elsewhere,²⁴ and is an accurate description of the beam provided the magnetic field is constant. However, when the beam propagates through an axially varying magnetic field, the parallel and perpendicular energy distributions become correlated due to conservation of energy and magnetic moment, leading to a deviation from the simple Gaussian and MB distributions given above. The *total* energy distribution, however, is unaffected by the changing magnetic field.

The effects of an axially varying magnetic field on the positron energy distributions may be examined by re-writing the joint distribution function, $f(E_{\parallel}, E_{\perp})$, in a magnetic field different from the field in which the beam was formed. Using conservation of energy and invariance of the positron magnetic moment, the joint distribution function of the beam as it propagates through an axially varying magnetic field may be written as

$$f(E'_{\parallel}, E'_{\perp}) = \frac{1}{\sqrt{2\pi} M k_b T_{\perp} \sigma_0} \times \exp\left[\frac{-E'_{\perp}}{M k_b T_{\perp}} - \frac{(E'_{\parallel} + E'_{\perp} (M-1)/M - \bar{E}_0)^2}{2\sigma_0^2}\right], \quad (8)$$

where M is the magnetic field ratio, defined as

$$M \equiv \frac{B'}{B_0} \quad (9)$$

with B_0 and B' the magnetic fields, where the beam is formed and measured, respectively. Note that in the limit $M \rightarrow 1$ (i.e., uniform field), $f(E'_{\parallel}, E'_{\perp}) \rightarrow f(E_{\parallel}, E_{\perp})$.

The parallel energy distribution of the beam as it propagates through an axially varying magnetic field can be obtained by integrating Eq. (8) over the perpendicular energy, yielding

$$f(E'_{\parallel}) = \frac{1}{2|\sigma_e|} \exp\left[\frac{1}{\sigma_e} \left(E'_{\parallel} + \frac{\sigma_0^2}{2\sigma_e} - \bar{E}_0\right)\right] \times \operatorname{erfc}\left[\frac{\operatorname{sgn}(M-1)}{\sqrt{2}\sigma_0} \left(E'_{\parallel} + \frac{\sigma_0^2}{\sigma_e} - \bar{E}_0\right)\right], \quad (10)$$

where

$$\sigma_e \equiv (M-1)k_b T_{\perp} \quad (11)$$

is the standard deviation of the exponential component of the distribution, and $\operatorname{sgn}(M-1)$ is $+1$ for $M > 1$ and -1 for $M < 1$. The mean and standard deviation of the overall parallel energy distribution can then be written as

$$\bar{E}'_{\parallel} = \bar{E}_0 + \sigma_e \quad (12)$$

and

$$\sigma'_{\parallel} = \sqrt{\sigma_0^2 + \sigma_e^2}. \quad (13)$$

Here, it is seen that, in general, the parallel energy distribution takes the form of an EMG distribution. In the limit that $M \rightarrow 1$ (uniform magnetic field), Eq. (10) simplifies to a Gaussian distribution, as described by Eq. (3). However, as the beam propagates through regions of lower ($M < 1$) or higher ($M > 1$) magnetic field, a tail develops on the right or left side of the distribution, respectively. Note that in the limit $M \rightarrow 0$, where all perpendicular energy has been transferred into the parallel, Eqs. (10)–(13) simplify to the total energy distribution given by Eqs. (5)–(7), showing that in this limit $E'_{\parallel} \rightarrow E_t$.

The perpendicular energy distribution in any magnetic field is obtained by integrating Eq. (8) over the parallel energy, giving

$$f(E'_{\perp}) = \frac{1}{2Mk_b T_{\perp}} \exp\left[-\frac{E'_{\perp}}{Mk_b T_{\perp}}\right] \times \operatorname{erfc}\left[\frac{1}{\sqrt{2}\sigma_0} \left(\frac{E'_{\perp}(M-1)}{M} - \bar{E}_0\right)\right]. \quad (14)$$

Here, it is seen that perpendicular energy distribution is no longer strictly a MB distribution when the beam propagates through an axially varying magnetic field. However, provided $\bar{E}_0 \gg \sigma_0$ (i.e., a relatively cold beam) and $M \ll \bar{E}_0/E'_{\perp}$, which ensures that no particles are reflected due to “magnetic mirroring,” Eq. (14) simplifies to a MB distribution characterized by a temperature $T'_{\perp} = MT_{\perp}$. In the limit $M \rightarrow 1$, Eq. (14) reduces to Eq. (4). In the limit of $M \ll 1$, Eq. (14) is equivalent to a MB distribution with $T'_{\perp} \ll T_{\perp}$, indicating that perpendicular energy has been transferred into the parallel.

In summary, the complete beam energy distribution functions at any magnetic field (i.e., M value) can be expressed analytically: Eq. (8) gives the joint distribution as a function of

both E'_{\parallel} and E'_{\perp} , while the single-variable distributions for the total, parallel, and perpendicular energies are given by Eqs. (5), (10), and (14), respectively. These expressions are expected to be useful in a number of applications, such as the analysis of trap-based beams and the study of elastic and inelastic scattering and annihilation processes.^{1,16,17}

C. Measurement and analysis techniques

The total energy and temporal distributions of the beam are important for a variety of applications. Narrow total energy distributions allow for more precise probing of physical processes, such as measurement of scattering cross sections and the study of VFRs. In contrast, narrow time pulses allow for more precise timing, providing better discrimination against background effects.

The temporal distribution of the beam is measured by allowing positrons ejected from the BGT to impinge upon, and subsequently annihilate at, a metal plate. The emitted gamma radiation is then measured as a function of time using a NaI detector. The response time of the NaI detector and associated electronics corresponds to a full-width at half-maximum (FWHM) of $\sim 0.5 \mu\text{s}$, which provides a non-negligible contribution to measurement of temporal distributions near or below this value. The measurement is fit to a Gaussian distribution, allowing the spread of the time distribution to be quantified.

An example of the measured temporal distribution is shown in Fig. 3. It should be noted that due to the small but finite parallel energy spread of the beam, the temporal spread varies as the beam propagates. Under typical conditions, the first positrons ejected have energies comparable to the magnitude of the exit-gate barrier, while those emitted later are lifted by the rising potential well, thus releasing them with greater energies. This can result in a temporal spread which converges as the beam propagates, due to the higher energy positrons catching up to those with lower energy released before them. However, experiments show no appreciable change in the time spread over the lengths available ($\sim 3 \text{ m}$), and simulations (discussed below) show that under the conditions described here, the beam is converging to a minimum $\sim 100 \text{ m}$ from the source. Thus, throughout this paper, the time spread will be treated as a constant.

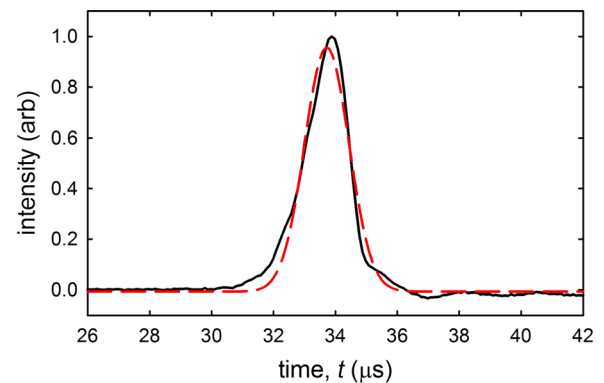


FIG. 3. (—) measured temporal distribution of a beam generated using $V_T = 30 \text{ V}$, $V_E = 3 \text{ V}$, and ramp parameters described in Fig. 2. (---) shows Gaussian fit, yielding a FWHM of $1.7 \mu\text{s}$.

The method used to measure the parallel energy distribution is shown schematically in Fig. 1. Positrons are ejected from the third stage of the BGT with a range of parallel energies. The beam is then passed through a retarding potential analyzer (RPA) electrode set to a potential V_A , allowing only particles with $E_{\parallel} > V_A$ to pass through and annihilate on a metal plate. The resulting gamma radiation is measured using a NaI detector. By repeating this procedure using a variety of RPA potentials, the average cumulative parallel energy distribution of the beam is constructed.

Experience has shown that the adsorption of molecules on the BGT and RPA electrodes produces potential offsets from the voltages set by the respective power supplies. These offsets depend upon the specific molecule and the electrode material (e.g., whether stainless steel, aluminum or gold-plated copper). One effect of this is that the mean beam energy measured using an RPA is found to shift as electrode surface conditions change. For example, measurements made before and after baking can show shifts in the mean beam energy of several electron-volts, while that measured in a nominally clean system typically drifts over time scales of days to weeks. These drifts are not problematic in typical experiments, since the measurements can be calibrated to account for these offsets (i.e., the RPA or scattering- or annihilation-cell cutoff measures accurately the zero of beam energy at that location).

An example of the measured cumulative parallel energy distribution is shown in Fig. 4(a). As discussed above, empirical measurements and simulations (discussed below) show

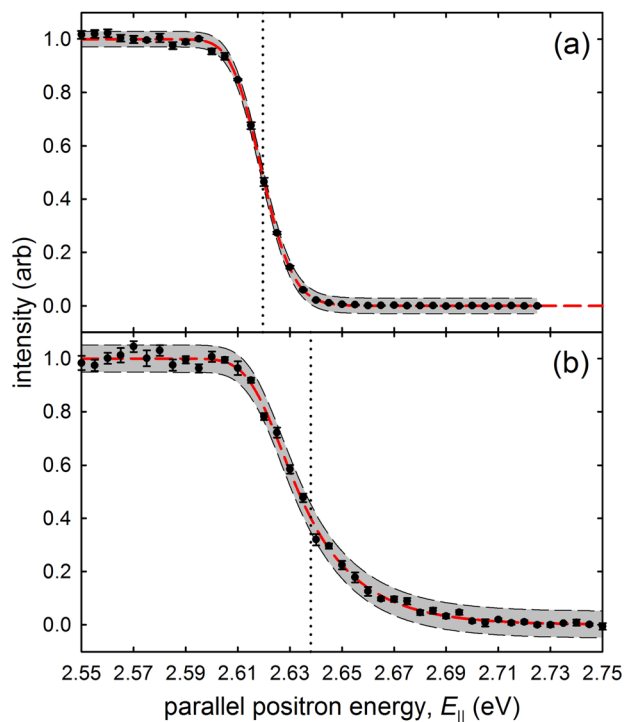


FIG. 4. Cumulative energy distributions (●) measured at an RPA magnetic field of (a) $B \sim 600$ G and (b) $B \sim 20$ G for the conditions described in Fig. 3. (—) EMG fit to data. Measurements done in (b) are at a sufficiently reduced field to effectively provide a measure of the total energy distribution. Shaded areas and vertical dotted lines show the 95% confidence intervals and mean parallel energies obtained from the fits. See text for details.

that in a uniform magnetic field, the parallel energy distribution closely resembles a Gaussian distribution, however, in general, it is described by an EMG distribution (c.f., Eq. (10)). For this reason, the data are fit to the cumulative distribution function of an EMG distribution, allowing the mean and standard deviation of the parallel energy distribution to be quantified, defined as in Eqs. (12) and (13), respectively.

The perpendicular energy distribution cannot be measured directly using the techniques described above. However, the *mean perpendicular energy* can be calculated using the measured parallel energy distribution, conservation of energy, and invariance of the magnetic moment. By measuring the parallel distribution at two different magnetic fields, the mean perpendicular energy of the beam can be calculated as

$$\bar{E}_{\perp} = \frac{\bar{E}'_{\parallel} - \bar{E}_{\parallel}}{1 - B'/B}, \quad (15)$$

where \bar{E}_{\perp} and \bar{E}_{\parallel} are the mean perpendicular and parallel energies at the RPA, B is the magnetic field in the RPA region, and the primes distinguish parameters evaluated at a different magnetic field. As discussed above, the perpendicular energies are assumed to be MB distributed at all times. Under this assumption, $\bar{E}_{\perp} = \sigma_{\perp} \equiv k_b T_{\perp}$, where σ_{\perp} is the standard deviation of the perpendicular energy distribution. This allows the perpendicular energy distribution to be fully characterized by Eq. (15).

While the constituent components have been discussed separately, the approximate total energy distribution can be measured directly, to a high degree of accuracy, using a variation of the technique for E_{\parallel} described above. As seen in Eq. (10), if the beam enters a region in which the magnetic field is small compared to that in the beam formation region, then the parallel energy distribution approaches the total energy distribution (i.e., the $M \rightarrow 0$ limit). Therefore, reducing the RPA magnetic field to a value small compared to the trapping magnetic field allows a direct measure of the total energy distribution to be made using the RPA procedure described above.

Figure 4(b) shows the measured cumulative “parallel” energy distribution with the RPA in a magnetic field reduced by a factor of 30 from that of the BGT, effectively measuring the total energy distribution. As in the parallel energy case, the measured total energy distribution is fit to an EMG distribution, allowing the mean and standard deviation to be quantified, defined as in Eqs. (6) and (7), respectively. The data fit very well to the EMG distribution, providing confirmation that the perpendicular energy distribution of the beam is indeed Maxwell-Boltzmann.

D. Measured beam energy distributions

An example of the measured parallel, perpendicular, and total energy distributions are shown in Fig. 5. The parallel and total distributions are the results of the EMG distribution function, using the fit parameters obtained from the measured cumulative distributions shown in Figs. 4(a) and 4(b). Equivalently, these curves may be obtained by taking the negative-derivative of the fits to the cumulative distributions shown in Fig. 4. The

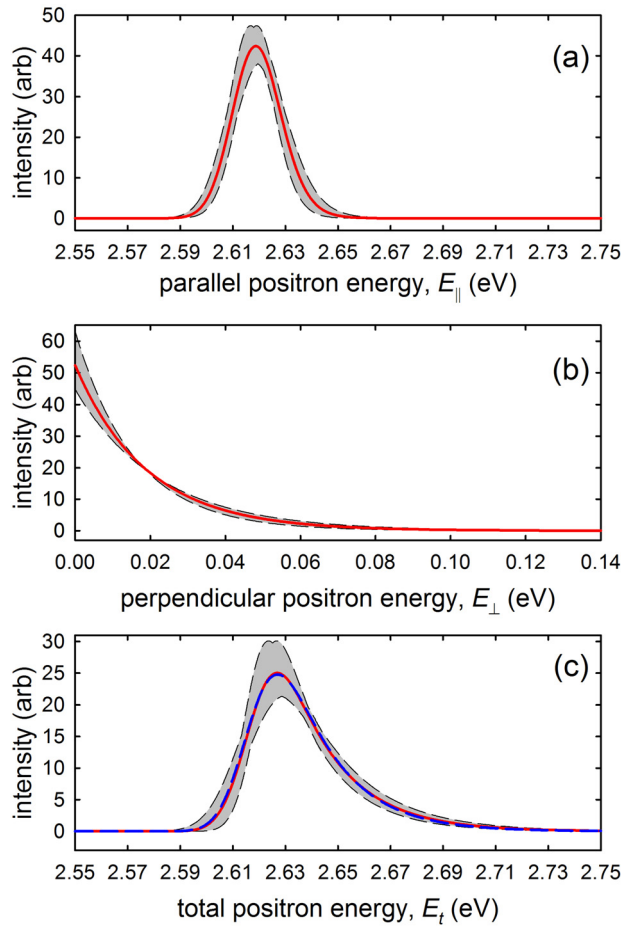


FIG. 5. Beam distributions obtained from the fits shown in Fig. 4: (a) parallel energy distribution resulting from Eq. (10) using $\sigma_{\parallel} = 9.7$ meV and $\bar{E}_{\parallel} = 2.620$ eV obtained from fit to data in Fig. 4(a), (b) MB perpendicular energy distribution corresponding to the measured value of $\bar{E}_{\perp} = 19.1$ meV using Eq. (15), and (c) total energy distribution from (—) Eq. (5) using $\sigma_t = 22.5$ meV and $\bar{E}_t = 2.638$ meV obtained from fit to data in Fig. 4(b) and (---) result of the convolution of curves in (a) and (b). Shaded regions show 95% confidence intervals estimated from the fits.

perpendicular distribution is the result of Eq. (4) using the value for $\bar{E}_{\perp} = k_b T_{\perp}$ obtained from Eq. (15).

As an alternative to direct measurement, the total energy distribution can also be calculated using measurements of the parallel distribution at two different magnetic fields, enabling \bar{E}_{\perp} to be obtained using Eq. (15), and then convolving the measured parallel distribution with the MB characterized by $\bar{E}_{\perp} = k_b T_{\perp}$. The resulting convolution of the distributions shown in Figs. 5(a) and 5(b) is shown as the dashed line in Fig. 5(c). It is in excellent agreement with the direct measurement.

Spreads in the energy distributions are characterized here by their standard deviations. Fits to the distributions in Fig. 4 yield standard deviations of 9.7 and 22.5 meV for the parallel and total energy distributions, defined as in Eqs. (13) and (7), respectively, with a perpendicular energy spread of 19.1 meV, obtained using Eq. (15) and assuming a MB distribution (i.e., $\bar{E}_{\parallel} = \sigma_{\perp}$). Since the total energy of each positron is the sum of its parallel and perpendicular energies, the standard deviation of the total distribution can also be found from the parallel and perpendicular distributions by

$$\sigma_t = \sqrt{\sigma_{\parallel}^2 + \sigma_{\perp}^2 + 2\sigma_{\parallel,\perp}}, \quad (16)$$

where σ_{\parallel} and σ_{\perp} are the standard deviations of the parallel and perpendicular distributions, respectively, and $\sigma_{\parallel,\perp}$ is their covariance. For the case of a uniform B , the last term vanishes. However for the non-uniform fields considered here, the contribution is non-zero. Simulations indicate that setting $\sigma_{\parallel,\perp} = 0$ in Eq. (16) yields values of σ_t within 10% of those obtained by direct calculation from the simulated total energy distributions, indicating that $\sigma_{\parallel,\perp}$ can be neglected. We note that in earlier work,^{1,7,8,24} the effect of non-zero $\sigma_{\parallel,\perp}$ was neglected, and the full-width at half-maximum (FWHM) ΔE was quoted (in lieu of σ) using the correspondence $\Delta E = 2\sqrt{2\ln 2}\sigma$.

While σ_{\perp} may be obtained using Eq. (15), alternative methods of estimating σ_{\perp} are also available. Equation (16) may be re-written to allow calculation of σ_{\perp} by using the σ_{\parallel} and σ_t obtained from direct measurements and assuming $\sigma_{\parallel,\perp} = 0$. Additionally, the perpendicular energy spread may be obtained from the EMG fit to the measured total energy distribution, since $\sigma_{\perp} = k_b T_{\perp}$ from Eq. (5).

Three distinct methods for obtaining the spread in the total energy distribution of the positron beam have been described. The reduced-field RPA technique, the convolution of the measured parallel with a MB characterized by Eq. (15), and the estimation using Eq. (16) yield $\sigma_t = 22.5$, 21.6, and 21.4 meV, respectively, for the conditions shown in Fig. 5. Similarly, the perpendicular energy spread obtained using Eqs. (15), (16), and (5) yields $\sigma_{\perp} = 19.1$, 20.3, and 20.7 meV, respectively. The fact that these values agree to within $\pm 4\%$ provides further validation of the approximations made in the analyses described here.

To our knowledge, the data and analysis presented here represent the most accurate characterization of a pulsed, buffer-gas-trap based positron beam to date. However, they provide only limited information regarding the underlying physical mechanisms involved in this intrinsically dynamical process, and how one might modify the trap geometry and protocols to improve beam performance. Thus, in Sec. III, simulations are described that provide further insights.

III. SIMULATION OF BGT-BASED BEAMS

While the measurements described above allow characteristics of the beam to be studied, much of the dynamics of beam formation and ejection are difficult to study experimentally. On the other hand, since the final beam parameters depend on the relative trajectories of large numbers of positrons interacting with spatially and temporally varying electric fields, first-principles calculations are prohibitively difficult. For these reasons, simulations are used here to study the underlying physical processes.

A. Description of the simulations

Described here is a Monte-Carlo simulation that follows, in the guiding center approximation, the trajectories of a large number of particles through time-dependent potentials and static magnetic fields. The simulations assume

cylindrical symmetry and neglect space-charge, positron-positron, and positron-neutral effects. Experimental measurements show no significant dependence on positron number for the low densities used here, and beam-formation occurs on time scales which are fast compared to collision times, and so these effects are neglected. The externally applied potentials are allowed to vary axially, radially, and temporally; while the magnetic field B is allowed to vary axially, but is constant in time.

The positrons are initially placed within a potential well determined by the geometry of the trapping electrodes. The parallel and perpendicular velocities are described by 1-D and 2-D MB distributions, respectively, with the initial radial positions chosen to obey a Gaussian distribution. Initial axial positions of the positrons are generated to start the particles in a thoroughly mixed state. This is done by starting each positron in the center of the potential well with prescribed perpendicular and parallel velocities and radial position, and then allowing it to make 10 bounces in the well. The measured axial position distribution at the end of these bounces is used to determine the initial axial position distribution for the simulation. The parallel and perpendicular velocities are then adjusted, depending on the potential and magnetic field, to ensure the initial velocity distribution is MB distributed. This procedure ensures that the simulations begin with the particles in an equilibrium state in phase space (i.e., z and v_z).

Once the initial distributions have been determined, the axial positions and parallel velocities are calculated as the particle moves along the magnetic field line by numerically integrating the equations of motion using the velocity Verlet technique:²⁵

$$z(t + \delta t) = z(t) + v_{\parallel}(t)\delta t + \frac{1}{2m}F_{\parallel}(z, r, t)\delta t^2, \quad (17a)$$

$$v_{\parallel}(t + \delta t) = v_{\parallel}(t) + \frac{1}{2m}[F_{\parallel}(z, r, t) + F_{\parallel}(z, r, t + \delta t)]\delta t. \quad (17b)$$

Here, z is the axial position, δt is the integration time step, v_{\parallel} is the velocity parallel to the magnetic field, m is the positron mass, and F_{\parallel} is the force in the magnetic field direction.

For a positively charged particle with charge e in a potential ϕ and magnetic field B ,

$$F_{\parallel}(z, r, t) = -e \frac{d\phi(z, r, t)}{dz} - \frac{mv_{\perp}^2}{2B(z)} \frac{dB(z)}{dz}. \quad (18)$$

The first term is the force on the particle in a spatially varying potential, while the second term is the force on the positron orbital magnetic moment (c.f. Eq. (2)) due to the spatially varying B field.

The perpendicular velocity at any axial position can be determined using Eq. (2) as

$$v_{\perp}(z) = v_{\perp,0} \sqrt{\frac{B(z)}{B(z_0)}}, \quad (19)$$

where $v_{\perp,0}$ and z_0 are the initial perpendicular velocity and axial positions as determined from the initial distributions

described above. Additionally, variations in the axial magnetic field, dB/dz , lead to a non-zero radial magnetic field component which results in a radial drift to the positron guiding centers as they move in z ,

$$r(z) = r_0 \sqrt{\frac{B(z_0)}{B(z)}}, \quad (20)$$

where r_0 is the initial displacement of the guiding center from the axis of symmetry.

The positron trajectories can be determined using Eqs. (17)–(20) as the particles interact with the varying potential and magnetic field. For the simulations here, the trajectories of 20 000 positrons were followed for each simulation. The externally applied potentials $\phi(z, r, t)$ are calculated as a function of z , r , and t on a grid of 0.05 cm, 0.25 cm, and 5 ns, respectively, using a finite-element method and the experimental electrode geometry. The magnetic fields $B(z)$ are defined on-axis only, using an axial step size of 0.05 cm. The numerical integration was done using a time step δt of 1 ns. Reducing this time step by an order of magnitude had no significant effect on the results, indicating that stable numerical solutions were reached.

B. Dynamics during beam formation

The simulation parameters chosen throughout this paper are intended to replicate the experimental conditions as accurately as possible. The initial parallel and perpendicular velocities are chosen to form 1-D and 2-D MB distributions at 300 K (unless otherwise noted), with the initial radial positions Gaussian-distributed with a FWHM of 0.5 cm ($\sigma = 0.21$ cm). The externally applied potentials due to voltages on the electrodes are calculated using realistic electrode geometry, and $B(z)$ is taken directly from experimental measurements (c.f. Fig. 6(c)).

Figure 6 shows the initial conditions used in the simulation. The positrons are initially confined within the potential well generated by the trapping-gate, well, and exit-gate electrodes, here set to 30, 0, and 3 V, respectively. They are allowed to bounce within the well for 10 μ s to verify that they remain MB distributed at their initial temperature, after which the pulsed beam is formed at $t = 0 \mu$ s by increasing the well voltage according to Eq. (1) with $\tau_r = 10 \mu$ s.

The on-axis potential and positron positions at three different times during the ramp are shown in Fig. 7. At 16 μ s (Fig. 7(a)), the positrons are still confined within the potential well, but the well depth has decreased to ~ 75 mV. At 18.5 μ s (Fig. 7(b)), the well has become nearly flat, and some of the positrons have escaped, while the bulk of the positrons are ejected at $\sim 20 \mu$ s (Fig. 7(c)).

The beam formation process is highly dynamic in nature. The initial positron bounce time in the potential well is $\sim 1 \mu$ s, however this increases with time during the ramp, reaching $\sim 2 \mu$ s during the last bounce before ejection. While each positron makes ~ 12 bounces during the time the potential well is ramped, the final bounce has the largest impact on the resulting beam characteristics.

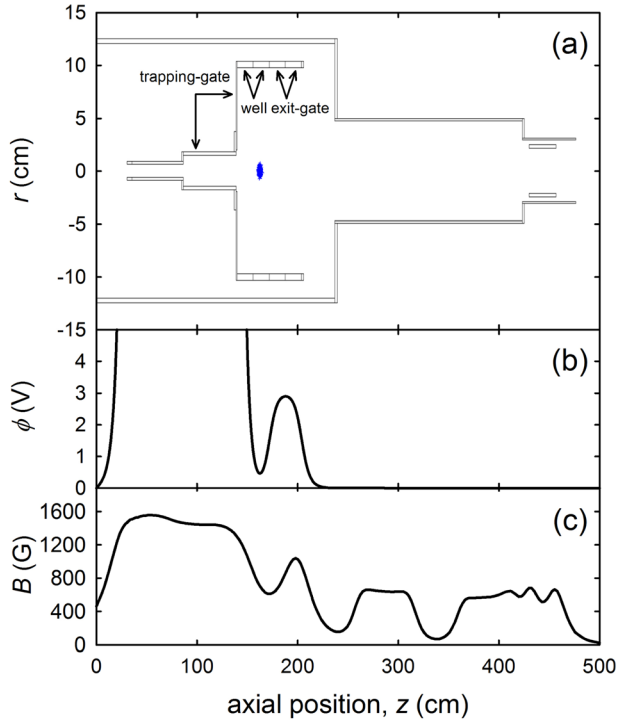


FIG. 6. (a) Electrode geometry with (●) positron initial axial and radial positions, (b) initial on-axis potential, and (c) axial magnetic field. For this example, the trapping-gate, well, and exit-gate electrodes are set to 30, 0, and 3 V, respectively.

Figure 8 shows the time dependence of important parameters during beam formation. The fraction of positrons remaining within the well is shown in Fig. 8(a), while the average well width w , calculated by averaging the width of the

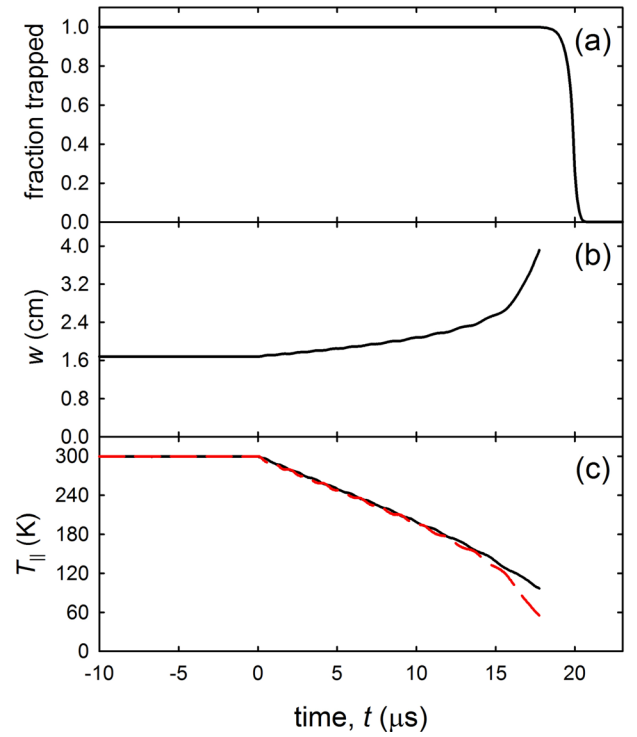


FIG. 8. (a) Fraction of positrons remaining in the trap, (b) average width w of the potential well as seen by the positrons, and (c) parallel positron temperature for the conditions described in Figs. 6 and 7. Red dashed line in (c) shows positron temperature obtained from Eq. (21) using $w(t)$ shown in (b).

well over positron energy at a given time, is seen in Fig. 8(b). The well width is a constant, w_0 , until $t = 0 \mu\text{s}$, at which time the well voltage is ramped according to Eq. (1), causing w to increase as the positrons are raised in the approximately parabolic well. As the well potential approaches the exit-gate potential, w increases dramatically, after which the potential becomes flat and the well disappears. Note that for the electrode geometry and potentials used here, few positrons are ejected from the trap until after $V_W > V_E$ and the well disappears (as seen by Fig. 8).

The parallel temperature during beam formation is shown in Fig. 8(c), obtained by fitting the parallel velocities of the positrons remaining within the well to a 1-D MB distribution. Here, it is seen that the parallel temperature decreases by a factor of ~ 3 during the beam formation process. This can be explained by conservation of the longitudinal adiabatic invariant, $J \sim v_{\parallel} w$, where w is the width of the potential well.²⁶ Expansion of the well during the ramp produces adiabatic cooling of T_{\parallel} . For comparison, the dashed line in Fig. 8(c) shows the calculated T_{\parallel} due to adiabatic cooling:

$$T_{\parallel}(t) = T_{\parallel,0} (w_0/w(t))^2, \quad (21)$$

where $T_{\parallel,0}$ is the initial parallel temperature and $w(t)$ is the average well width (i.e., shown in Fig. 8(b)). The two curves agree very well until the sudden increase in w just before the well vanishes. This occurs on time scales comparable to the positron bounce time, so that the longitudinal adiabatic invariant is no longer conserved.

The parallel cooling process during beam formation is beneficial to both the energy and time resolutions (as

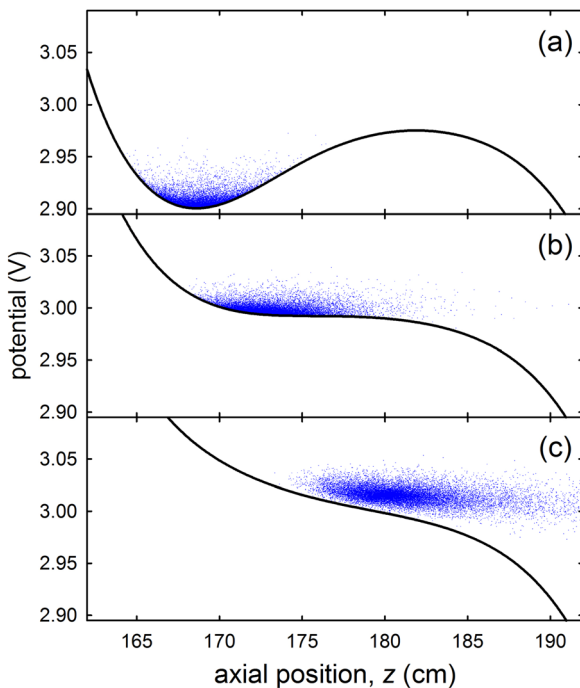


FIG. 7. (—) on-axis potential and (●) positron positions and energy at (a) $t = 16 \mu\text{s}$, (b) $t = 18.5 \mu\text{s}$, and (c) $t = 20 \mu\text{s}$ for the conditions described in Fig. 6, with the ramp function as in Eq. (1) with $V_s = 3.5 \text{ V}$, $V_0 = 0 \text{ V}$, and $\tau_r = 10 \mu\text{s}$.

discussed later), and by tailoring the initial potential well geometry and ejection conditions, this effect may be of further benefit. However, if beam formation occurs in a region of high neutral gas density (e.g., in some BGT's, particularly two-stage variations), formation and ejection must take place on time scales fast compared to the positron-neutral collision time scales, ensuring that the positrons are not re-heated during ejection, and slow compared to the positron axial bounce time, ensuring longitudinal adiabatic invariance is maintained. For the experiments described here, the positron-neutral collision time was ~ 1 ms, and so the effect of collisions is negligible during the $\sim 10 \mu\text{s}$ time required for beam formation.

C. Dynamics during beam transport

Once the positrons are ejected from the trap, they continue downstream in the spatially varying magnetic field. Figure 9 shows the axial and radial particle positions, the on-axis potential and magnetic field at $t = 22 \mu\text{s}$ for a simulation under the conditions described in Fig. 6. Here, the effects of the spatially non-uniform magnetic field are clearly seen as the radial expansion of the beam in regions of low B .

The parallel, perpendicular, and total energy are calculated for each particle at each axial location. To compare with experimental results, the beam energy distributions are recorded in the RPA region, while the temporal distribution is calculated at the location of the annihilation plate. Random time-dependent voltage fluctuations with a root-mean-squared (rms) voltage of 7 mV were added to the potential of each electrode, and the distributions are obtained by taking the average of 50 separate simulations. This

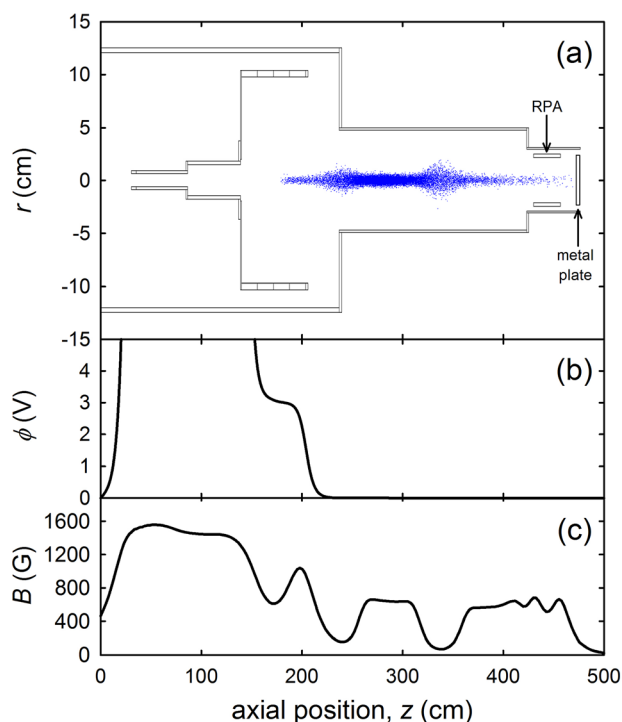


FIG. 9. (a) Electrode geometry with (●) positron axial and radial positions, (b) on-axis potential, and (c) on-axis magnetic field at $t = 22 \mu\text{s}$ under the conditions described in Fig. 6 and 7.

process most accurately replicates the conditions and procedures used to experimentally measure the energy distribution using the RPA technique described earlier. Finally, the temporal distributions are convolved with a $0.5 \mu\text{s}$ FWHM ($\sigma = 0.21 \mu\text{s}$) Gaussian distribution to account for the detector response. The consequences of these additional effects, which are relatively minor under most conditions, are discussed further below.

IV. EXPERIMENT AND SIMULATIONS: COMPARISONS AND PARAMETER STUDIES

In this section, experimental and simulation results for the temporal and energy distributions of the beams are compared and the effects of varying the initial conditions and ejection parameters are discussed. Since the experimental geometry is necessarily fixed (i.e., electrode dimensions and positions), the principal parameters affecting beam quality are the initial positron temperature and the imposed variation of electrode potential as a function of time in the region of the trapping well. For the experimental data shown, the error bars are based on the propagated standard error obtained from their respective fits.

A. Beam distributions

The beam distributions obtained under the experimental and simulation conditions described by Figs. 2–9 are shown in Fig. 10. As discussed in Sec. II, arbitrary shifts in the energy axis are present in the experimental energy measurements, therefore the experimental parallel and total energy measurements shown here have been shifted along the x-axis to match the peaks in the simulations. For the simulations shown in Fig. 10, the standard deviations are 9.0, 21, and 23 meV for the parallel, perpendicular, and total energy distributions, and $0.26 \mu\text{s}$ for the temporal distribution. For comparison, the respective experimental values are 9.7, 19.1,

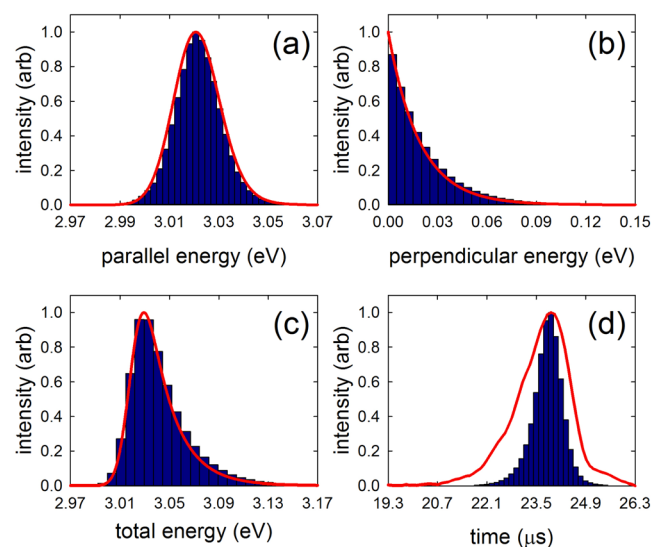


FIG. 10. Beam distributions for the conditions described by Figs. 2–9. (a) Parallel energy, (b) perpendicular energy, (c) total energy, and (d) time. Blue bars represent simulation results, and red lines show experimental measurements. See text for details.

and 22.5 meV for the energy spreads, and $0.71 \mu\text{s}$ for the time spread.

The simulated parallel, perpendicular, and total energy distributions agree extremely well with the measured distributions. However, the measured temporal distribution is significantly broader than the simulation results, though the shape is qualitatively consistent. Unfortunately, the reason for this discrepancy is unclear, though a similar effect was seen by Tattersall *et al.*²⁷ Experiments and simulations show that non-uniformities in the (presumed smooth) exit-gate potential can substantially broaden the time spread by reflecting some fraction of the positrons during ejection, therefore requiring them to make additional bounces within the well. Experiments were done to minimize the effects of these non-uniformities, and yielded reductions in the time spreads similar in magnitude to the discrepancy seen here. Additionally, experimental measurements show a moderate dependence of the temporal spread on the number of positrons, suggesting positron-positron effects may be important. These effects are still under investigation.

B. Dependence on ejection rate

In order to study the effects of varying the *dynamics* of the ejection process, the initial well geometry is held fixed, while the time dependence of the voltage applied to the well electrode is varied. For the data presented here, the trapping and exit-gate electrodes were held at 30 and 3 V, respectively, with the well electrode initially at ground.

Referring to the ramp function given by Eq. (1), two parameters affect how fast the positrons are ejected from the trap without affecting the initial well geometry: the steady-state voltage V_s and the RC time τ_r . Experimentally, τ_r is set by the resistance and capacitance of the amplifier-electrode circuit, while V_s is the steady-state voltage applied to the well electrode. The effect of varying the latter is discussed here.

While the positrons have typically long exited the trap before the ramp reaches V_s , its value changes the time at which $V_W \sim V_E$ (and therefore the slope of the voltage ramp, see Fig. 2). For this reason, an important quantity is the height the well is raised above the exit-gate potential, called here the ramp voltage, $\Delta V_r = V_s - V_E$.

Figure 11(a) shows the standard deviation of the parallel energy distribution as the ramp voltage is varied. The simulation results agree well with the experimental measurements, with both showing a similar increase in parallel energy spread as ΔV_r is increased. This increase is due to the potential well lifting the positrons above the exit-gate potential during the last bounce before being ejected from the trap. The first positrons to be ejected leave the trap with parallel energies comparable to the exit-gate potential, while successively ejected positrons are lifted above it (c.f. Fig. 7), adding to the parallel energy spread. This effect is more pronounced at higher ramp voltages, leading to the increase in σ_{\parallel} with Δ_r .

Because the perpendicular energy is not affected by the beam formation process, it remains constant (~ 20 meV) as the ramp voltage is varied. Consequently, changes in the

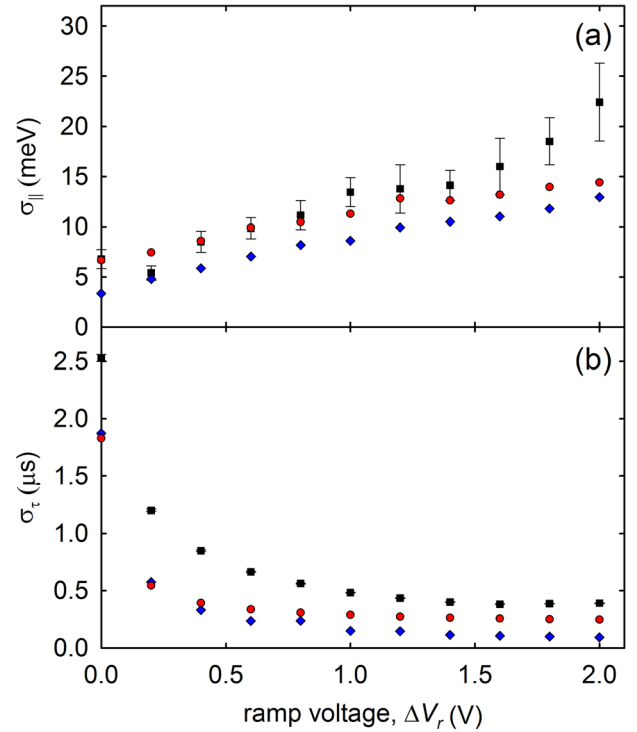


FIG. 11. Standard deviations of the (a) parallel energy and (b) time distributions using various ramp voltages, $\Delta V_r = V_s - V_E$, at $V_T = 30$ V, $V_E = 3$ V, and $\tau_r = 10 \mu\text{s}$. (■): experimental measurements, (●): simulation results, and (◆): simulation results without the nominal 7 mV rms electronic noise and broadened NaI detector response.

total energy spread depend only on the parallel spread. As discussed earlier, the total energy spread may be approximated using Eq. (16) once the parallel and perpendicular spreads are known.

The dependence of σ_{τ} on the ramp voltage is shown in Fig. 11(b). As discussed earlier, the simulations yield smaller time spreads than those measured experimentally. However, the simulations and measurements show a similar trend with changes in ΔV_r , namely, larger ΔV_r values yield smaller time spreads. This can be explained by the same mechanism described above. The later a positron is ejected from the trap, the more quickly it is accelerated out of the trap by the raising potential. Therefore, the higher the ramp voltage, the smaller the time between the first and last positron ejected, and so the smaller the time spread.

Under this mechanism, the parallel-energy and time spreads are oppositely affected. Larger ramp voltages lead to smaller time spreads and larger energy spreads; while smaller ramp voltages lead to smaller energy spreads and larger time spreads. While varying the ejection dynamics cannot improve both of these parameters simultaneously, it does allow one of these parameters (at a time) to be optimized for a particular application.

Also shown in Fig. 11 are the simulation results without the effects of the 7 mV rms electrical noise and detector response. Here, it is seen that the contribution from the noise is typically a small fraction of the parallel energy spread, particularly at higher ramp voltages where the parallel energy spreads are larger. However, for beams generated using low ramp voltages, as much as 50% of the parallel

energy spread is due to this noise, indicating that minimizing electronic noise may be necessary for optimum parallel energy resolution.

The mechanism by which electronic noise broadens the parallel energy spread depends on the time scale of the noise. For electronic fluctuations on time scales short compared to positron ejection times, the noise acts to provide additional fluctuations in the parallel energy of each positron, thereby increasing the parallel energy spread of a given pulse. Alternatively, if the noise occurs on time scales long compared to the ejection time, the noise contributes the same random perturbation to the energies of *all* of the positrons in a given pulse, thus shifting the mean parallel energy. Over multiple pulses, these random shifts cause a broadening of the *average* parallel energy distribution.

While σ_τ is not affected by the presence of electronic noise, the detector response affects the temporal distribution in cases where the time spread is small. This contribution is relatively large at high ramp voltages, broadening the time spread by as much as a factor of ~ 3 ; however, it is insufficient to account for the discrepancy between the measured and simulated temporal distributions (c.f. Fig. 11(b)). Furthermore, the breadth of the temporal distribution is as large or larger at low ramp voltages, where effects due to detector response are negligible

C. Dependence on initial temperature

For the experiments and simulations described here, the applied trapping-gate voltage, initial well voltage, and exit-gate voltages were kept the same as above, 30, 0, and 3 V, respectively, with the ramp function as in Eq. (1) with $V_s = 3.5$ V and $\tau_r = 10$ μ s. Experimentally, the positrons were allowed to cool on N_2 for a variable amount of time. Molecular nitrogen was used as the primary cooling gas, rather than CF_4 , for more precise control of the final positron temperature (due to slower cooling times). The positron temperature was then measured using the procedure described in Ref. 28 to obtain beam parameters at a variety of temperatures ≥ 300 K. In the simulations, the initial parallel and perpendicular velocity distributions are taken to be 1-D and 2-D MB distributions at the specified temperature.

As discussed earlier, simulations show that the final parallel temperature of the trapped positrons is lower than the initial parallel temperature due to the presence of adiabatic cooling during beam formation. As the initial temperature is varied, the final temperature reached also varies, keeping the ratio of these values approximately constant. The perpendicular temperature is unaffected by this process.

Figure 12 shows the energy and time spreads as the positron temperature is varied. Here, as in the case described above, the simulated and measured σ_{\parallel} are in good agreement. The increase in σ_{\parallel} with temperature can be explained by inspection of the allowed trajectories as the positrons are lifted out of the potential well. Particles with higher parallel velocities are able to explore a larger region of the potential well. This results in a wider variety of trajectories, and hence a greater variety of final energies, thus increasing σ_{\parallel} .

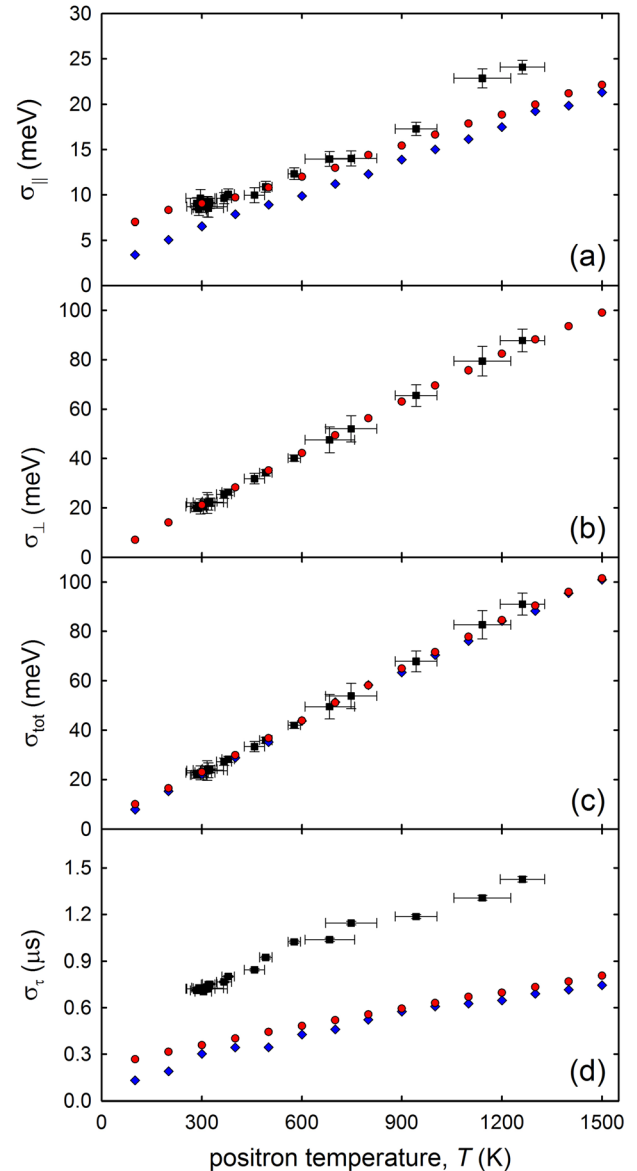


FIG. 12. Standard deviation of (a) parallel energy, (b) perpendicular energy, (c) total energy, and (d) time distributions of positron beam generated at different initial positron temperatures: (■) experimental measurements; (●) simulation results; and (◆) simulation results without the 7 mV RMS electronic noise and broadening due to NaI detector response.

At low temperatures, for example, the positrons have a small spread in parallel velocities, which also limits the available axial positions explored. Therefore, the distribution of axial positions when the positrons have sufficient energy to overcome the exit-gate barrier is narrower, resulting in the positrons exiting the trap with a smaller range of energies.

The perpendicular energy spread is shown in Fig. 12(b). Not surprisingly, σ_{\perp} is proportional to the positron temperature. Had the magnetic field been uniform (i.e., equal in magnitude in the BGT and RPA), σ_{\perp} would be equal to $k_b T$. However, in the case considered here, the magnetic field is non-uniform, particularly in the region where the beam is formed (c.f. Figs. 6 and 9), resulting in $\sigma_{\perp} \sim 0.8 k_b T$ due to perpendicular energy transferred into parallel by invariance of the orbital magnetic moment.

As shown in Fig. 12(c), the total energy spread is dominated by σ_{\perp} over the temperature range studied. This can be seen from Eq. (16) in the limit $\sigma_{\perp} \gg \sigma_{\parallel}, \sigma_{\parallel, \perp}$. Thus, for beams with $\sigma_{\parallel} \ll k_b T$, reducing T is a particularly effective method for improving the total energy spread.

Finally, Fig. 12(d) shows the effect of positron temperature on the temporal spread of the beam. As discussed above, the simulations under-predict σ_{τ} as compared to the experimental measurements. However, the overall trend is the same: reducing positron temperature yields a smaller time spread. The mechanism invoked to explain the dependence of σ_{\parallel} on temperature also provides a consistent explanation of the temporal behavior. At higher temperatures more positrons have sufficient energy to be trapped higher in the potential well, thus allowing them to be ejected earlier (i.e., when $V_W \approx V_E$), and increasing the time spread.

These results show that reducing the temperature of the initial positron cloud is an effective way to improve both the energy and time resolution. In fact, combining this result with the effects of varying the ramp voltage, discussed in Sec. III, could provide an additional reduction of either the energy or time spread. In particular, adjusting the ramp voltage, such that either the time or energy spread remains constant as the temperature is reduced, will result in additional improvements to the chosen distribution beyond simply varying the temperature.

Also shown in Fig. 12 are simulation results without the 7 mV RMS electronic noise and minimum detector response. As in Sec. III, the impact of the noise is most significant at very low parallel energy spreads, contributing $\sim 30\%$ of the parallel energy spread at 300 K. Since the total energy spread is dominated by the perpendicular spread under these conditions, and electronic noise has no effect on the perpendicular energy, the effect of electronic noise on the total energy spread σ_{τ} is quite small. Similarly, the broadening of the temporal distribution σ_{τ} due to the detector response is relatively small over the temperature range studied.

V. CONCLUDING REMARKS

Experimental measurements, analytic expressions, and simulation results for the formation of pulsed, magnetically guided positron beams have been presented. The results show that the beam formation process is intrinsically dynamic; each positron follows a different trajectory, interacting with a different potential that depends upon its initial conditions. The effective width of the potential well increases during the voltage ramp, causing the parallel velocities of the trapped positrons to decrease through adiabatic cooling. This leads to an increase in the average particle bounce time and a significant reduction in parallel temperature. Thus, large improvements to both the parallel energy and time spreads can be obtained by tailoring the potential well to provide the maximum change in well width during the ramp.

The effect of varying the rate at which the positrons are ejected from the trap was also studied. Increasing the ramp voltage, defined as the difference in voltage between the well and exit-gate electrode at the end of the ramp, leads to

an increase in the parallel energy spread and a decrease in the temporal spread. Both effects arise from the increased change in potential during the time the positrons are being ejected, accelerating the last particles more and ejecting them faster and to higher energies than earlier particles.

Change of the initial temperature was also investigated. Decreasing T results in a smaller phase space for the positrons, limiting the height reached within the potential well and forcing a larger majority to follow similar trajectories during the potential ramp, thus reducing both the time and parallel energy spreads. Since the perpendicular energy is not affected by the beam formation process, T_{\perp} is reduced in proportion to the change in temperature. Combining the benefits of temperature and ramp-voltage optimization can provide significantly improved beam quality for a range of applications.

The mechanism responsible for the apparent broadness of the temporal spreads is still unclear. While the shape of the distribution and its dependence on operating parameters are in qualitative agreement with the simulations, a narrower distribution is predicted in all cases. As discussed earlier, experiments and simulations suggest that this effect may be due to non-uniformities in the exit-gate potential, and this will continue to be investigated.

The analytic expressions for the beam energy distributions, developed here for trap-based, magnetically guided positron beams, are expected to be useful in a number of applications, including the analysis of beam energy distributions and also in the study of elastic and inelastic scattering and annihilation processes.

Many interesting processes and interactions involving positrons have yet to be studied experimentally due to limitations in current technology. Examples include study of low energy and/or narrow features that require substantial improvements in energy resolution. The more complete understanding of the beam formation process developed here can potentially lead to such improvements. To this end, simulations are in progress to explore further the effects of varying parameters, such as electrode geometry, details of the potential well and ejection protocols.²⁹ It is hoped that this will aid in the development of improved techniques to study low-energy positron-matter interactions.

ACKNOWLEDGMENTS

We wish to acknowledge the expert technical assistance of E. A. Jerzewski. This work is supported by the U.S. National Science Foundation, Grant Nos. PHY 10-68023 and 14-01794.

¹G. F. Gribakin, J. A. Young, and C. M. Surko, *Rev. Mod. Phys.* **82**, 2557 (2010).

²N. Guessoum, P. Jean, and W. Gillard, *Mon. Not. R. Astron. Soc.* **402**, 1171 (2010).

³*Principles and Practice of Positron Emission Tomography*, edited by R. L. Wahl (Lippincott Williams & Wilkins, Philadelphia, PA, 2002).

⁴D. W. Gidley, H.-G. Peng, and R. S. Vallery, *Annu. Rev. Mater. Sci.* **36**, 49 (2006).

⁵P. G. Coleman, *Positron Beams and Their Applications* (World Scientific, 2000).

⁶A. P. Mills and E. M. Gullikson, *Appl. Phys. Lett.* **49**, 1121 (1986).

⁷S. J. Gilbert, C. Kurz, R. G. Greaves, and C. M. Surko, *Appl. Phys. Lett.* **70**, 1944 (1997).

- ⁸C. Kurz, S. Gilbert, R. Greaves, and C. Surko, *Nucl. Instrum. Methods Phys. Res., Sect. B* **143**, 188 (1998).
- ⁹T. J. Murphy and C. M. Surko, *Phys. Rev. A* **46**, 5696 (1992).
- ¹⁰M. Amoretti *et al.*, *Nature* **419**, 456 (2002).
- ¹¹G. Gabrielse *et al.*, *Phys. Rev. Lett.* **89**, 213401 (2002).
- ¹²G. B. Andresen *et al.*, *Nature* **468**, 673 (2010).
- ¹³G. Gabrielse *et al.*, *Phys. Rev. Lett.* **108**, 113002 (2012).
- ¹⁴D. B. Cassidy and A. P. Mills, *Nature* **449**, 195 (2007).
- ¹⁵D. Chaudhary, M. Went, K. Nakagawa, S. Buckman, and J. Sullivan, *Mater. Lett.* **64**, 2635 (2010).
- ¹⁶C. M. Surko, G. F. Gribakin, and S. J. Buckman, *J. Phys. B: At. Mol. Opt. Phys.* **38**, R57 (2005).
- ¹⁷J. P. Sullivan, S. J. Gilbert, J. P. Marler, R. G. Greaves, S. J. Buckman, and C. M. Surko, *Phys. Rev. A* **66**, 042708 (2002).
- ¹⁸J. Marler, G. Gribakin, and C. Surko, *Nucl. Instrum. Methods Phys. Res., Sect. B* **247**, 87 (2006).
- ¹⁹A. C. L. Jones, J. R. Danielson, M. R. Natisin, C. M. Surko, and G. F. Gribakin, *Phys. Rev. Lett.* **108**, 093201 (2012).
- ²⁰A. C. L. Jones, J. R. Danielson, M. R. Natisin, and C. M. Surko, *Phys. Rev. Lett.* **110**, 223201 (2013).
- ²¹J. R. Danielson, A. C. L. Jones, M. R. Natisin, and C. M. Surko, *Phys. Rev. A* **88**, 062702 (2013).
- ²²A. P. Mills, Jr., *Appl. Phys.* **22**, 273 (1980).
- ²³T. R. Weber, J. R. Danielson, and C. M. Surko, *Phys. Plasmas* **15**, 012106 (2008).
- ²⁴G. F. Gribakin and C. M. R. Lee, *Phys. Rev. Lett.* **97**, 193201 (2006).
- ²⁵W. C. Swope, H. C. Andersen, P. H. Berens, and K. R. Wilson, *J. Chem. Phys.* **76**, 637 (1982).
- ²⁶D. H. E. Dubin and T. M. O'Neil, *Rev. Mod. Phys.* **71**, 87 (1999).
- ²⁷W. Tattersall, R. D. White, R. E. Robson, J. P. Sullivan, and S. J. Buckman, *J. Phys.: Conf. Ser.* **262**, 012057 (2011).
- ²⁸M. R. Natisin, J. R. Danielson, and C. M. Surko, *J. Phys. B* **47**, 225209 (2014).
- ²⁹M. R. Natisin, J. R. Danielson, and C. M. Surko, "Optimization of trap-based positron beams" (unpublished).